


# Synthesis, characterizations, electrochemical and molecular docking studies of $Co_xFe_{1-x}Fe_2O_4/Fe_2O_3$ nanoparticle

M. I. M. Ismail, Hassen Harzali, HaikelHrichi, Hasan A. El-adawy, Khaled A. Abdelshafeek, and Ahmed A. Elhenawy

**Citation:**Chin. Phys. B, 2025, 34 (**10**): 108202. DOI: 10.1088/1674-1056/adde35
http://cpb.iphy.ac.cn; http://iopscience.iop.org/cpb

**What follows is a list of articles you may be interested in**

---

## Magnetic properties of oxides and silicon single crystals

Zhong-Xue Huang(黄忠学), Rui Wang(王瑞), Xin Yang(杨鑫), Hao-Feng Chen(陈浩锋), and Li-Xin Cao(曹立新)
Chin. Phys. B, 2022, 31 (**8**): 087501. DOI: 10.1088/1674-1056/ac70c2

## Relationship between ESIPT properties and antioxidant activities of 5-hydroxyflavone derivates

Chaofan Sun(孙朝范), Bifa Cao(曹必发), Hang Yin(尹航), Ying Shi(石英)
Chin. Phys. B, 2020, 29 (**5**): 058202. DOI: 10.1088/1674-1056/ab7ea1

## Theoretical study on the relationship between the position of the substituent and the ESIPT fluorescence characteristic of HPIP

Xin Zhang(张馨), Jian-Hui Han(韩建慧), You Li(李尤), Chao-Fan Sun(孙朝范), Xing Su(苏醒), Ying Shi(石英), Hang Yin(尹航)
Chin. Phys. B, 2020, 29 (**3**): 038201. DOI: 10.1088/1674-1056/ab6d50

## Low temperature ferromagnetic properties of CdS and CdTe thin films

Hafiz Tariq Masood, Zahir Muhammad, Muhammad Habib, Dong-Ming Wang(王东明), De-Liang Wang(王德亮)
Chin. Phys. B, 2017, 26 (**6**): 067503. DOI: 10.1088/1674-1056/26/6/067503

---

# Synthesis, characterizations, electrochemical and molecular docking studies of $Co_xFe_{1-x}Fe_2O_4/Fe_2O_3$ nanoparticle

M. I. M. Ismail[1,2,†], Hassen Harzali[3,4], HaikelHrichi[2,5], Hasan A. El-adawy[3,7], Khaled A. Abdelshafeek[3,6], and Ahmed A. Elhenawy[3,7]

[1] *Department of Physics, Faculty of Science, Port Said University, Port Said, Egypt*
[2] *Department of Physics, Faculty of Sciences, Al-Baha University, Al-Baha* 65731, *KSA*
[3] *Department of Chemistry, Faculty of Sciences, Al-Baha University, Al-Baha* 65731, *KSA*
[4] *Applied Mineral Chemistry Laboratory (LR*19*ES*02*), Department of Chemistry, Faculty of Sciences of Tunis, Tunis El Manar University, Tunis, Tunisia*
[5] *Laboratory of Interfaces and Advanced Materials, Faculty of Science, University of Monastir, Monastir* 5019, *Tunisia*
[6] *Pharmaceutical Industries and Drugs Institute, Chemistry of Medicinal Plants Department, National Research Center, ElBohouth Street, Dokki, Giza* 12622, *Egypt*
[7] *Department of Chemistry, Faculty of Science, Al-Azhar University, Cairo, Egypt*

(Received 9 March 2025; revised manuscript received 12 May 2025; accepted manuscript online 29 May 2025)

The advantageous magnetic, optical, and antibacterial properties of magnetic nanoparticles have recently drawn a lot of attention in the field of biomedicine. One of the most famous super paramagnetic materials, nanoferrite, is made up of two types of spinel structures: inverse and normal. Cobalt ferrite's inverse spinel structure offers several benefits, including excellent magnetostrictivity, good coupling efficiency, and inexpensive cost. This study's objective is to synthesize, characterize, and investigate the characteristics of the electrochemical properties of $Co_xFe_{1-x}Fe_2O_4/Fe_2O_3$ ($x = 0.30$ and 0.77) nanoparticles using the chemical co-precipitation method. The physical properties of the produced nanoparticles were investigated using x-ray diffraction (XRD), transmission electron microscopy (TEM), and a vibrating sample magnetometer (VSM). The band gap properties of magneto-nano powders, including the direct and indirect band gap energies, and Urbach energy, are found. Scanning electron microscopy showed the presence of spherical nanoparticles ranging from 20.7 nm–23.7 nm. The analysis of $Co_xFe_{1-x}Fe_2O_4/Fe_2O_3$ ($x = 0.30$ and 0.77) nanoparticles, for instance, reveals differences in their surface characteristics that are significant for their potential applications. Parameters like $d_{\text{norm}}$, $d_e$, and $d_i$, along with shape index and curvedness, contribute to a comprehensive understanding of the molecular surface, which is crucial for the design of new materials with desired physical and chemical properties. Molecular docking studies have revealed promising interactions between certain crystals and DNA gyrase, mirroring the binding mode of known inhibitors. This suggests potential for these crystals to serve as antimicrobial agents in future research. Such findings are crucial as they contribute to the development of new treatments against antibiotic-resistant bacteria, a growing global health concern.

**Keywords:** magnetic nanoparticles, cobalt ferrite, energy gap, electrochemical assessments, molecular docking

**PACS:** 82.45.Rr, 75.20.–g, 71.20.Ps, 71.30.+h

**DOI:** 10.1088/1674-1056/adde35 **CSTR:** 32038.14.CPB.adde35

## 1. Introduction

In many facets of life, nanotechnology research and use are expanding rapidly. Many researchers were drawn to the ever-growing possibilities of magnetic nanoparticles, particularly nanoferrites. The most important and extensively researched magnetic nanoparticle among them is cobalt ferrite nanoparticles. Reducing occupational and environmental hazards required the use of environmentally friendly synthetic technologies.[1–4] Inductors, drug delivery systems, microwave reflection, humidity sensors, electrical designs, and magnetic resonance imaging are just a few of the technological fields that heavily rely on ferrites. Ferrites are also utilized in high-density data storage, converters, antenna bodies, and catalysts.[5–8]

Ferrites can be coupled with divalent metallic ions (e.g., $Co^{2+}$, $Ni^{2+}$, $Zn^{2+}$) to enhance their structural and magnetic properties.[9] For instance, cobalt ions are known to promote magneto-crystalline anisotropy in spinel ferrites by mediating superexchange interactions between $Fe^{3+}$ and $Co^{2+}$ ions at octahedral sites, thereby increasing coercivity.[10] Due to its unique and versatile physical characteristics, cobalt ferrite ($CoFe_2O_4$; CFO) has been extensively studied for the last fifty years. These traits render CFO exceptionally promising across diverse fields, including catalyst research, nanobiotechnology, data storage, magneto-electronics, optoelectronics, and highly sensitive sensors.[11–13] In 2023, Dabagh *et al*. and Gheidari *et al*. developed spinel ferrite nanoparticles with significant antibacterial properties attributed to metal substitution.[14,15]

[†]Corresponding author. E-mail muhammad_398@yahoo.com

© 2025 Chinese Physical Society and IOP Publishing Ltd. All rights, including for text and data mining, AI training, and similar technologies, are reserved.

These composites can be used in many different antibacterial applications and are safe, affordable, and eco-friendly. The chemical co-precipitation method was employed by El Ghandoor *et al.*[16] to create MF and $Fe_3O_4$ nanoparticles. This procedure makes use of a novel 1:2 $Fe^{2+}$ to $Fe^{3+}$ ratio using $(NH_4)_2Fe(SO_4)_2$ as the ferrous source. Many authors prepared ($Fe_3O_4$) as pure phase or ($M_xFe_{3-x}O_4$), where $M$ can be any bivalent metal, by altering the Fe/$M$ ratio.[17–19]

## 2. Experimental procedures

### 2.1. Synthesis of $Co_xFe_{1-x}Fe_2O_4/Fe_2O_3$ ($x = 0.30$ and 0.77) nanoparticle

Temperature, pH of the suspension, and the initial molar concentration reaction all have a major impact on the magnetization of substituted ferrite nanoparticles.[20,21] $(NH_4)_2Fe(SO_4)_2$, $CoSO_4{\cdot}7H_2O$, and $FeCl_3$ were co-precipitated in an alkaline media to yield ultrafine nanoparticles of $Co_yFe_{1-y}Fe_2O_4$ ($y = 0.25$ and 0.75). Unfortunately, during the synthesi, some of the $Fe^{2+}$ in $(NH_4)_2Fe(SO_4)_2$ was oxidized to $Fe^{3+}$. This led to a deviation in the feed ratio and the formation of $Co_xFe_{1-x}Fe_2O_4/Fe_2O_3$ ($x = 0.30$ and 0.77), which will be confirmed in Subection 3.1. In the case of synthesizing $Co_{0.25}Fe_{0.75}Fe_2O_4$ nanoparticles, which were diverted to synthesize $Co_{0.30}Fe_{0.70}Fe_2O_4/Fe_2O_3$ 150 ml of 0.5-M $(NH_4)_2Fe(SO_4)_2$, 50 ml of 0.5-M $CoSO_4{\cdot}7H_2O$, and 100 ml of 2-M $FeCl_3$ were combined and kept at 80 °C. These mixtures are added to a boiling NaOH solution (0.5 mol of dissolved NaOH is present in 600 ml of distilled water) and stir for ten seconds. Metal salts quickly change into hydroxides, which subsequently turn into ferrites, to generate nanoferrites. The solutions are maintained at 100 °C for 1.5 hours. The other $Co_{0.75}Fe_{0.25}Fe_2O_4$ nanoferrite is synthezied in the same way, but by using 50 ml of 0.5-M $(NH_4)_2Fe(SO_4)_2$, 150 ml of 0.5-M $CoSO_4{\cdot}7\ H_2O$ and 100 ml of 2-M $FeCl_3$. But again, the ferrous ions are oxidized, and the ratio is deflected to form particles $Co_{0.77}Fe_{0.23}Fe_2O_4/Fe_2O_3$ nanoparticles.

Before being divided into three parts, the particles of $Co_xFe_{1-x}Fe_2O_4/Fe_2O_3$ ($x = 0.30$ and 0.77) are thoroughly cleaned with distilled water. In the first part, the particles are immersed in distilled water without any additional ingredients; in the second part, they are dried at 100 °C for an hour; and in the third part, they are centrifuged and re-dispersed in oleic acid, which acts as a liquid carrier to prepare MFs from the nanoparticles of $Co_xFe_{1-x}Fe_2O_4/Fe_2O_3$ ($x = 0.30$ and 0.77).

### 2.2. Identification of $Co_xFe_{1-x}Fe_2O_4/Fe_2O_3$ ($x = 0.30$ and 0.77) nanoparticles

#### 2.2.1. The x-ray diffraction analysis

Using a Philips X'Pert XRD device with Cu $K\alpha$ radiation ($\lambda = 1.54056$ Å) at 40 kV and 30 mA, the second part of the prepared samples were examined to measure the lattice strain, lattice parameter, average particle size, and interplanar spacing of $Co_xFe_{1-x}Fe_2O_4/Fe_2O_3$ ($x = 0.30$ and 0.77) nanoparticles.

#### 2.2.2. Transmission electron microscopy

Using a TEM (Jeol_Jem_1230 electron microscope), the microstructure and particle size of $Co_xFe_{1-x}Fe_2O_4/Fe_2O_3$ ($x = 0.30$ and 0.77) nanoparticles were investigated. For this test, the first components produced during the synthesis stage were employed.

#### 2.2.3. Magnetization measurement

Magnetization studies were carried out using a home-made VSM on the second part of $Co_xFe_{1-x}Fe_2O_4/Fe_2O_3$ ($x = 0.30$ and 0.77) nanoparticles at an ambient temperature up to a maximum magnetic field ($H$) of 9000 Oe (1 Oe = 79.5775 A/m). The specific saturation magnetization ($M_S$), coercive force ($H_c$), and remanence ($M_r$) were all evaluated.

#### 2.2.4. Spectrophotometric measurements of MFs

The optical absorption of particles $Co_xFe_{1-x}Fe_2O_4/Fe_2O_3$ ($x = 0.30$ and 0.77) in the form of (MFs) was measured in the third part using a spectrophotometer (Unicam UV-2). From the optical absorption results, each optical energy gap of the direct ($E_{G1}$) and indirect ($E_{G2}$) transition occurring in the band gap, as well as Urbach energy EU, could be determined.

#### 2.2.5. Computational methodology

Calculations using density functional theory (DFT), especially with the Jaguar package,[22] are essential for making very accurate predictions about the structures and characteristics of molecules. For these kinds of simulations, the B3LYP/6-311G**(d,p)[23] exchange–correlation functional is a common choice, providing detailed insights into molecular geometry and electronic distributions. Time-dependent DFT (TD-DFT) further extends these capabilities, allowing for the exploration of excited states and electronic transitions. The use of Hirshfeld surface analysis like Crystal Explorer enhances the understanding of intermolecular interactions, offering a visual and quantitative assessment of crystal packing and bonding patterns.

#### 2.2.6. Computational approach to protein–ligand interaction analysis

Computational methods for analyzing protein–ligand interactions have attracted the attention of researchers.[24,25] Recently, a highly sensitive electrochemical sensor based on protein-templated split aptamer ligation reaction has been developed.[24,25]

Starting with the acquisition of a three-dimensional (3D) protein structure from the Protein Data Bank, the workflow includes assigning charges and bond orders, adding hydrogen atoms, and modifying amino acids. The OPLS force field is

applied for protein minimization, ensuring the structure's stability within a specified 0.30-Å RMSD. Identification of binding pockets (12 Å × 12 Å × 12 Å into an active site) using CASTp allows for examination of potential ligand interactions. Subsequently, the Glide software facilitates the creation of a receptor grid, leading to a docking simulation that meticulously evaluates ligand poses for the best fit within the protein's active site, culminating in a Glide score that reflects the binding affinity.

## 3. Results and discussion

### 3.1. The x-ray powder diffraction analysis

Figure 1 displays the x-ray diffraction patterns of the dried $Co_xFe_{1-x}Fe_2O_4/Fe_2O_3$ ($x = 0.30$ and 0.77) nanoparticles. The diffraction peaks' locations and intensities correspond to the conventional pattern for JCPDS card No. (22-1086) $CoFe_2O_4$.[26]

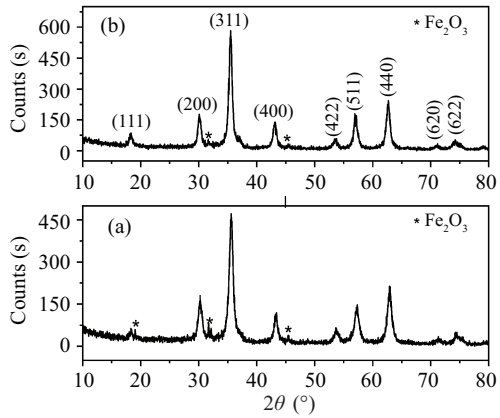



**Fig. 1.** The XRD pattern of (a) $Co_{0.30}Fe_{0.70}Fe_2O_4/Fe_2O_3$ and (b) $Co_{0.77}Fe_{0.23}Fe_2O_4/Fe_2O_3$ nanoparticles.

Figure 1 further reveals distinct peaks at $2\theta = 19.01°$, 31.78°, and 45.49° (marked by stars), indicating the formation of an unintended $Fe_2O_3$ phase during the synthesis of $Co_yFe_{1-y}Fe_2O_4$ ($y = 0.25$ and 0.75) nanoparticles. These peaks are more pronounced in $Co_{0.30}Fe_{0.7}Fe_2O_4/Fe_2O_3$ but less intense in $Co_{0.77}Fe_{0.23}Fe_2O_4/Fe_2O_3$, correlating with the reduced $(NH_4)_2Fe(SO_4)_2$ concentration. The ICDD matching (JCPDS 391346) confirms $Fe_2O_3$ formation,[27] suggesting partial $Fe^{2+}$ oxidation during synthesis. The deviation from the feed ratio (original Co content $x$) stems from preferential $Co^{2+}$ incorporation into the spinel lattice, leaving excess $Fe^{3+}$ to form $Fe_2O_3$ — a phenomenon documented in co-precipitated ferrites.[28] To quantify phase segregation, the $Fe_2O_3$ peak intensity at 31.78° was compared to the primary spinel peak (35.5°, (311)), enabling estimation of the revised Co content ($x_a$). Table 1 reflects this adjusted stoichiometry. The presence of prominent peaks in $Co_xFe_{1-x}Fe_2O_4/Fe_2O_3$ ($x = 0.30$ and 0.77) nanoparticles indicate that the particles are extremely fine and have small crystallite sizes less than 25-nm crystallites. Nano-sized powders of $Co_xFe_{1-x}Fe_2O_4/Fe_2O_3$ ($x = 0.30$ and 0.77) nanoparticles have been successfully obtained. The Debye–Scherrer formula states that the average particle size $D_{hkl}$ for $Co_xFe_{1-x}Fe_2O_4/Fe_2O_3$ ($x = 0.30$ and 0.77) determined by[29]

$$D_{hkl} = 0.9\lambda/\beta\cos\theta. \tag{1}$$

The formula denotes the wavelength ($\lambda$) as 0.154056 nm, the half diffraction angle of $2\theta$ (Bragg angle), and $\beta$ is the full width at half maximum (FWHM) value of the XRD diffraction lines (Fig. 1). The particle size is calculated by averaging the sizes at $D_{220}$, $D_{311}$, $D_{400}$, $D_{422}$, $D_{511}$, and $D_{440}$ peaks.

Bragg's law determines the lattice parameter $a_o$ and the interplanar spacing $d_{hkl}$ (Eqs. (2) and (3)) respectively.[30] The values of the interplanar spacing $d_{311}$ are listed in Table 1

$$d_{hkl} = \lambda/2\sin\theta, \tag{2}$$

$$d_{hkl} = a_o/\sqrt{h^2+k^2+l^2}. \tag{3}$$

By plotting $\sqrt{h^2+k^2+l^2}$ as a function of $1/d_{hkl}$ for all samples. The lattice parameters $a_o$ are calculated by taking the slopes of these curves see Fig. 2, the correlation coefficient ($R^2$) for the samples is 0.999, indicating a strong fit of the data to the formula The lattice parameter values are listed in Table 1. By graphing, for each sample, $\sqrt{h^2+k^2+l^2}$ as a function of $1/d_{hkl}$. The slopes of these curves are used to determine the lattice parameters $a_o$ (see Fig. 2). The correlation coefficient ($R_2$) for the samples is 0.999, showing a good fit between the data and the formula. Table 1 lists the values of the lattice parameters.

Table 1 makes it evident that the lattice parameter falls with increasing $Co^{2+}$ concentration. The ionic radius of $Co^{2+}$ is (0.072 nm),[31] whereas that of $Fe^{2+}$ is (0.077 nm).[32] It is well known that the substitution of $Co^{2+}$ for $Fe^{2+}$ results in a drop in the unit cell volume, which in turn produces a decrease in the lattice parameter.

**Table 1.** Original cobalt content ($y$), accurate cobalt content ($x$), $Fe_2O_3$ %, interplanar spacing $d_{311}$, $a_o$, average crystallite size estimated from XDR (CS), average particle size estimated from TEM (PS), $M_s$, $M_r$, $H_c$, $E_{G1}$, $E_{G2}$, and $E_U$ of $Co_xFe_{1-x}Fe_2O_4/Fe_2O_3$ ($x = 0.30$ and 0.77) nanoparticles.

| $y$ | $x$ | $Fe_2O_3$ (%) | $d_{311}$ (Å) | $a_o$ (Å) | CS (nm) | PS (nm) | $M_s$ (emu/g) | $M_r$ (emu/g) | $H_c$ (Oe) | $E_{G1}$ (eV) | $E_{G2}$ (eV) | $E_U$ (eV) |
|---|---|---|---|---|---|---|---|---|---|---|---|---|
| 0.25 | 0.30 | 14.5 | 2.5229 | 8.3750 | 15.2 | 20.77 | 51.3 | 4.10 | 150 | 2.72 | 1.0 | 0.63 |
| 0.75 | 0.77 | 9.10 | 2.5216 | 8.3461 | 18.9 | 23.73 | 56.6 | 7.25 | 70 | 2.50 | 0.9 | 0.77 |

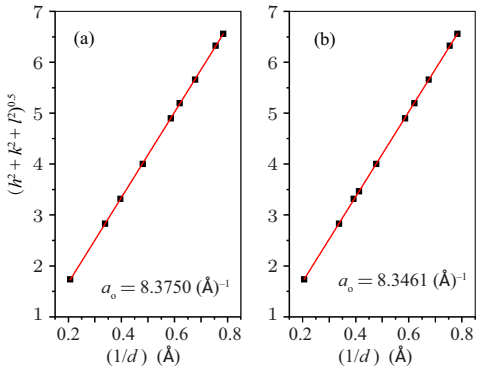



**Fig. 2.** The $\sqrt{h^2+k^2+l^2}$ versus $(1/d)$ of (a) $Co_{0.30}Fe_{0.70}Fe_2O_4/Fe_2O_3$ and (b) $Co_{0.77}Fe_{0.23}Fe_2O_4/Fe_2O_3$ nanoparticles.

### 3.2. Transmission electron microscopy

High-resolution TEM is used for direct observation and examination of the morphology of $Co_xFe_{1-x}Fe_2O_4/Fe_2O_3$ ($x = 0.30$ and 0.77) nanoparticles. Figure 3 displays the micrographs of $Co_xFe_{1-x}Fe_2O_4/Fe_2O_3$ ($x = 0.30$ and 0.77) nanoparticles. The tested particles have a narrow size distribution and are all spherical and closely match the sizes predicted by Eq. (1), are shown in Table 1.

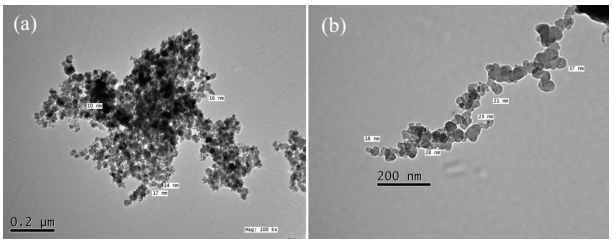



**Fig. 3.** Transmission electron micrograph of (a) $Co_{0.30}Fe_{0.7}Fe_2O_4/Fe_2O_3$ and (b) $Co_{0.77}Fe_{0.23}Fe_2O_4/Fe_2O_3$ nanoparticles.

### 3.3. Magnetic characterization of $Co_xFe_{1-x}Fe_2O_4/Fe_2O_3$ ($x = 0.30$ and 0.77) nanoparticles

Using VSM, the magnetic properties of the room-temperature generated nanocrystals are investigated. Figure 4 (ferrite $M$–$H$ curves) displays the magnetization, $M$ (in units of emu/g), against the applied magnetic field, $H$ (in units of Oe). Based on data from Fig. 5, Table 1 displays the current samples' $H_C$, $M_S$, and $M_r$.

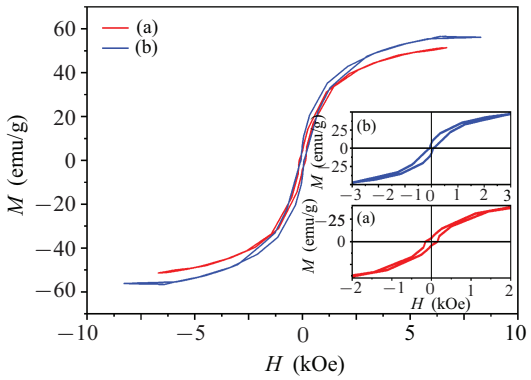



**Fig. 4.** Room temperature hysteresis loop for (a) $Co_{0.30}Fe_{0.70}Fe_2O_4/Fe_2O_3$ and (b) $Co_{0.77}Fe_{0.23}Fe_2O_4/Fe_2O_3$ nanoparticles.

Table 1 shows that $M_s$ of $Co_{0.77}Fe_{0.23}Fe_2O_4/Fe_2O_3$ (56.6 emu/g) is larger than $M_s$ of $Co_{0.30}Fe_{0.7}Fe_2O_4/Fe_2O_3$ (51.3 emu/g) this can be explained by the increase of crystalline size,[33,34] also as $Fe_2O_3$ increases magnetization decreases. $M_r$ significantly increases when the quantities of cobalt in the samples rise. Figure 4 shows that as cobalt concentration increases the area of hysteresis increases because of the anisotropy property of cobalt. Figure 4 clearly shows that the hysteresis loop has vanished, indicating that the sample is superparamagnetic. Upon examining Fig. 4 and consulting Ref. [35], it is simple to regard $Co_xFe_{1-x}Fe_2O_4$ ($x = 0.30$ and 0.77) as soft magnetic materials.

### 3.4. Spectrophotometric measurements of $Co_xFe_{1-x}Fe_2O_4/Fe_2O_3$ ($x = 0.30$ and 0.77) MFs

Using a scanning range of wavelengths from 190 nm to 1000 nm and a scanning interval of 0.2 nm, the optical absorption ($A$) of $Co_xFe_{1-x}Fe_2O_4/Fe_2O_3$ ($x = 0.30$ and 0.77) is presented in Fig. 5. The Urbach energy and the optical energy band gaps of the direct and indirect transitions that take place in the band gap can be found using the optical absorption data.

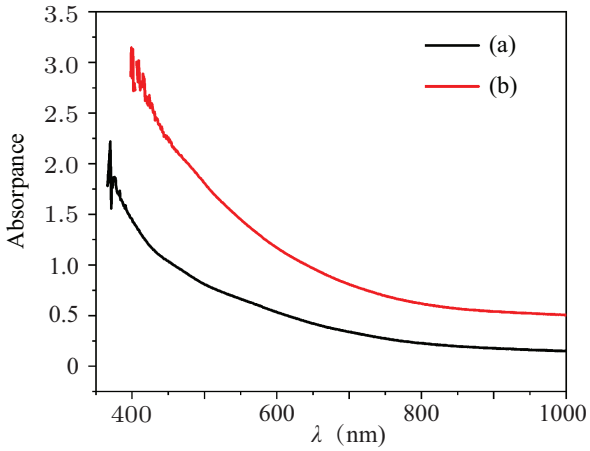



**Fig. 5.** The absorbance $A$ versus the wavelength $\lambda$ (in units of nm) of (a) $Co_{0.30}Fe_{0.70}Fe_2O_4/Fe_2O_3$ and (b) $Co_{0.77}Fe_{0.23}Fe_2O_4/Fe_2O_3$ MFs.

#### 3.4.1. Determination of direct and indirect optical energy band gap of $Co_xFe_{1-x}Fe_2O_4Fe_2O_3$ ($x = 0.30$ and 0.77) MFs

An equation for the absorption coefficient, $\alpha(\nu)$, as a function of photon energy ($h\nu$) for both direct and indirect transition using Eq. (4) was provided by Davis and Mott[36]

$$\alpha(\nu) = \alpha_o(h\nu - E_G)^n/h\nu. \tag{4}$$

The absorption coefficient is represented by $\alpha(\nu)$, $\alpha_o$ is a constant that indicates the band tailing extent; the optical energy band gap is represented by $E_G$; the permitted direct transition is denoted by $n = 1/2$, while the permitted indirect transition is represented by $n = 2$.

The optical energy band gap for the direct $E_{G1}$ transition and the indirect $E_{G2}$ transition can be found by graphing $(h\nu\alpha)^2$ and $(h\nu\alpha)^{1/2}$ versus photon energy $(h\nu)$, respectively.

As seen in Figs. 6 and 7, the corresponding values of $E_G$ are found by extrapolating $(h\nu\alpha)^2 = 0$ for direct transition and $(h\nu\alpha)^{1/2} = 0$ for indirect transition. Table 1 presents the results.

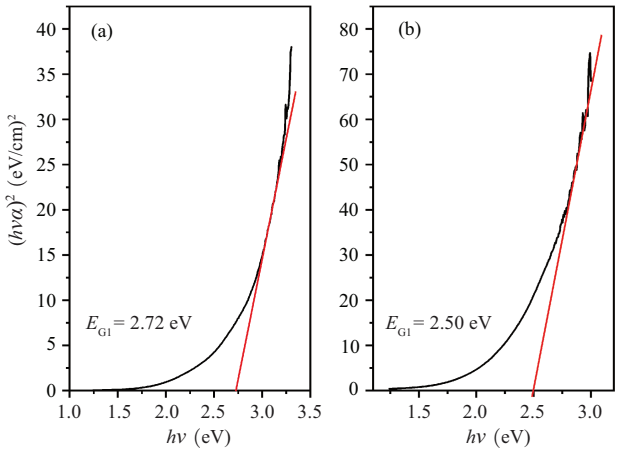



**Fig. 6.** The optical energy band gap determination for direct transition $E_{G1}$ of (a) $Co_{0.30}Fe_{0.70}Fe_2O_4/Fe_2O_3$ and (b) $Co_{0.77}Fe_{0.23}Fe_2O_4/Fe_2O_3$ MFs.

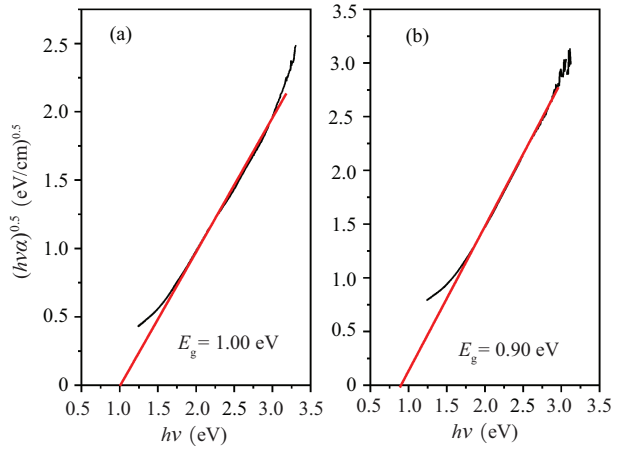



**Fig. 7.** The optical energy band gap determination for indirect transition $E_{G2}$ of (a) $Co_{0.30}Fe_{0.70}Fe_2O_4/Fe_2O_3$ and (b) $Co_{0.77}Fe_{0.23}Fe_2O_4/Fe_2O_3$ MFs.

The degree to which the data fits the formula for either $n = 1/2$ or $n = 2$ is shown by the correlation coefficient, which in this instance is 0.997. A perfect match is shown by $R^2 = 1$. Based only on $R^2$ measurements, it is difficult to identify whether magnetic fluids contain an indirect or direct band gap. However, it should be noted that the analogous indirect band gap values are lower than the direct band gap values. The content of cobalt in the samples determines the values of the direct and indirect band gaps. As cobalt concentration increases the energy gap, even though direct or indirect decreases this is because cobalt has one electron more than iron in the outer valance level which increases the repulsion forces in cobalt more than iron which facilitates transferring the cobalt electrons more than iron electrons, i.e., lowering the energy gap of cobalt comparing with iron. It is also known that the smaller the crystal size, the higher the energy gap band,[37] which was also confirmed by the current results.

The values of both direct and indirect energies band gaps of magnetic fluids $Co_xFe_{1-x}Fe_2O_4/Fe_2O_3$ ($x = 0.30$ and 0.77) are classified as semiconductors, semiconductors energies band gaps (0 eV–3 eV).[38]

#### 3.4.2. Determination of $E_U$ of $Co_xFe_{1-x}Fe_2O_4/Fe_2O_3$ ($x = 0.30$ and 0.77) MFs

Urbach energies are given by empirical relations[39]

$$\alpha(\nu) = \beta \exp(h\nu/E_U), \tag{5}$$

where $\nu$ is the radiation frequency, $E_U$ is the Urbach energy, which represents the width of the band tails of the localized state and is a constant. Figure 8 shows the calculated Urbach energies of $Co_xFe_{1-x}Fe_2O_4/Fe_2O_3$ ($x = 0.30$ and 0.77) by taking the reciprocals of the slopes of the liner portion in the lower photon energy of the curves representing the relationship between the photon energy ($h\nu$) and the logarithm of the absorption coefficient, $\ln(\alpha)$. The Urbach energies of $Co_{0.30}Fe_{0.7}Fe_2O_4/Fe_2O_3$ and $Co_{0.77}Fe_{0.23}Fe_2O_4/Fe_2O_3$ are found to be 0.63 eV and 0.77 eV, respectively. This indicates that there is less energetic disorder at the band edges of $Co_{0.30}Fe_{0.70}Fe_2O_4/Fe_2O_3$ than there is in $Co_{0.77}Fe_{0.23}Fe_2O_4/Fe_2O_3$.

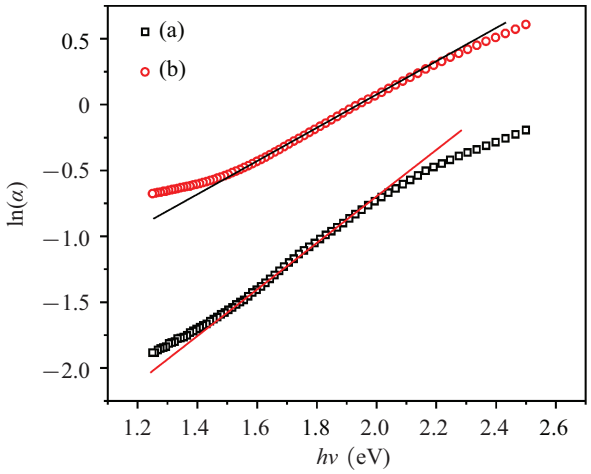



**Fig. 8.** The logarithm of the absorption coefficient, $\ln(\alpha)$, against photon energy, ($h\nu$), for panel (a) $Co_{0.30}Fe_{0.70}Fe_2O_4/Fe_2O_3$ and panel (b) $Co_{0.77}Fe_{0.23}Fe_2O_4/Fe_2O_3$ MFs.

### 3.5. Structural properties for crystal

The structural and intermolecular characteristics of the synthesized $Co_xFe_{1-x}Fe_2O_4/Fe_2O_3$ nanoparticles (where the accurate cobalt content, $x$, is 0.30 and 0.77) were meticulously investigated using 3D Hirshfeld surface analysis. This computational technique, performed using the Crystal Explorer software package[40] with a high standard resolution and an isovalue of 0.5 for surface generation (as depicted in Fig. 9), allows for the partitioning of crystal space into molecular volumes and provides a powerful means to visualize and quantify intermolecular interactions. Key molecular attributes derived

from this methodology include not only overall shape descriptors such as volume, surface area, globularity (a measure of sphericity, where 1.0 is a perfect sphere), and a sphericity (deviation from a sphere), but also detailed mapping of close contact interactions.[41]

The Hirshfeld surface analysis revealed significant differences in the surface properties of the nanoparticles contingent on the cobalt substitution level ($x$). For the $Co_{0.30}Fe_{0.70}Fe_2O_4/Fe_2O_3$ nanoparticles, the analysis indicated a structure that deviates considerably from perfect sphericity. While possessing a globularity index of 0.602, suggesting a somewhat compact but non-spherical form, its surface volume of 175.17 Å$^3$ and surface area of 193.51 Å$^2$ point towards a degree of structural asymmetry.

In contrast, data presented for $Co_{0.77}Fe_{0.23}Fe_2O_4/Fe_2O_3$ compound exhibits internal contradictions that require clarification. One set of reported values suggests a larger surface volume (614.83 Å$^3$) and a slightly larger surface area (196.61 Å$^2$) compared to the $Co_{0.30}$ sample, with a notably higher globularity of 0.825, indicative of a more spherical structure.[42] However, a subsequent statement, it was similarly noted that the $Co_{0.77}Fe_{0.23}Fe_2O_4/Fe_2O_3$ compound's globularity value of 0.798 suggests a nearly spherical structure, with a deviation of 0.031, albeit with a smaller surface volume 417.01 Å$^3$ and area 157.64 Å$^2$ than $Co_{0.30}Fe_{0.7}Fe_2O_4/Fe_2O_3$ presents a different set of parameters: a globularity of 0.798 (with an unrelated "spherical structure 0.031" value that appears erroneous), a surface volume of 417.01 Å$^3$, and an area of 157.64 Å$^2$. This second set of data implies a smaller volume and area than the $Co_{0.30}$ sample and contradicts the first set for the $Co_{0.77}$ sample.

Assuming a consistent data set can be established, such quantitative measurements of molecular shape and volume are crucial for understanding how these nanoparticles might interact with biological systems or pack in condensed phases, thereby influencing their macroscopic properties and potential applications. The Hirshfeld surface itself, as visualized in Fig. 9 for the $Co_xFe_{1-x}Fe_2O_4/Fe_2O_3$ systems ($x = 0.30$ and 0.77), is mapped with several key parameters to deconstruct the nature of intermolecular contacts. The normalized contact distance ($d_{norm}$) is a particularly insightful parameter. It is calculated based on $d_e$ (the distance from a point on the surface to the nearest nucleus external to the surface) and $d_i$ (the distance from a point on the surface to the nearest nucleus internal to the surface), normalized by the van der Waals radii of the respective atoms. The $d_{norm}$ surface provides a color-coded map. Red regions indicate negative $d_{norm}$ values, signifying intermolecular contacts shorter than the sum of van der Waals radii, often corresponding to stronger interactions like hydrogen bonds or significant close contacts. Blue regions represent positive $d_{norm}$ values, indicating contacts longer than van der Waals separations, typical of weaker interactions. White regions denote $d_{norm}$ values close to zero, where contacts are approximately at the van der Waals separation. This detailed mapping provides a nuanced understanding of the specific atomic interactions driving crystal packing and stability. Further elucidating the surface topology are the shape index and curvedness parameters. The shape index quantifies the local curvature of the Hirshfeld surface, ranging typically from −1.0 (concave, like a hole) to +1.0 (convex, like a sphere). Color-coding based on shape index (red for concave, blue for convex) highlights regions of shape complementarity between interacting molecules, which is essential for understanding packing motifs and recognition phenomena. The curvedness parameter, ranging from approximately −4.0 Å to +0.4 Å (though units vary based on definition), provides information on the "flatness" or "sharpness" of the surface regions. Low curvedness values (closer to zero) correspond to relatively flat, disc-like areas, while high positive values indicate sharp edges or protrusions, and high negative values indicate deep indentations. These features are indicative of the strength and directionality of interactions; for instance, large flat patches might suggest significant $\pi$–$\pi$ stacking if aromatic systems are involved, or generally weaker, less specific van der Waals/dispersion interactions that dominate crystal packing in the absence of strong directional forces. Collectively, these Hirshfeld surface-derived parameters offer a comprehensive, visual, and quantitative framework for analyzing the complex landscape of intermolecular interactions within the crystal structures of these nanomaterials,[43] which is fundamental to understanding their formation, stability, and potential functional behavior in various applications.

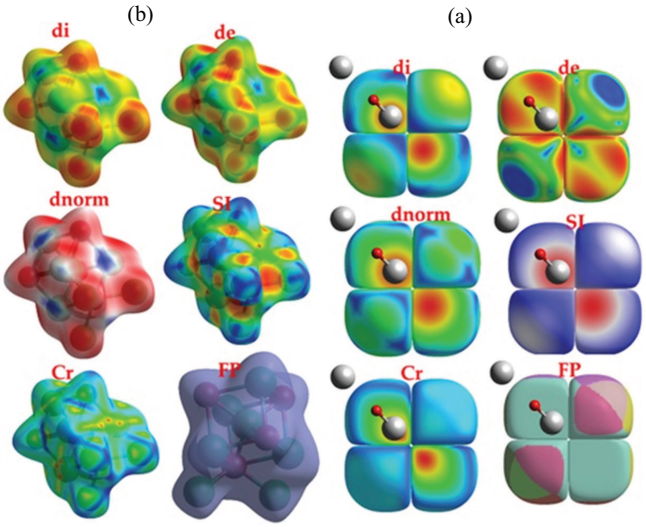



**Fig. 9.** The Hirshfeld surface for (a) $Co_{0.30}Fe_{0.70}Fe_2O_4/Fe_2O_3$ and (b) $Co_{0.77}Fe_{0.23}Fe_2O_4/Fe_2O_3$ nanoparticles mapped with $d_{norm}$, $d_i$, $d_e$ shape index, curvedness, and Fragment patches.

### 3.6. Molecular docking profile

This work evaluated the antibacterial activity of $Co_{0.77}Fe_{0.23}Fe_2O_4/Fe_2O_3$ crystal as a sample example on DNA gyrase using molecular docking techniques. The crystal compound interacted with the same residues as the control within the active site of the enzyme, as indicated by the PDB identification 6RKS.[44] After self-docking had generated the first positions, induced-fit docking produced the final docking poses. These final poses were reduced using the OPLS force field, with selection criteria based on the lowest binding free energy (BE) and the lowest root-mean-square deviation (RMSD) between the refined and initial postures. The highest binding effectiveness (BE) served as the selection criterion. The docking data suggests that the crystals may interact with key amino acids in the protein's active area through a range of interaction types, including hydrogen bonds, arene–cation contacts, and arene–arene interactions. Notably, it was shown that significant amino acids including F225, N226, Q214, C195, and Y136 were implicated in the binding pocket, as figure 10 depicts.

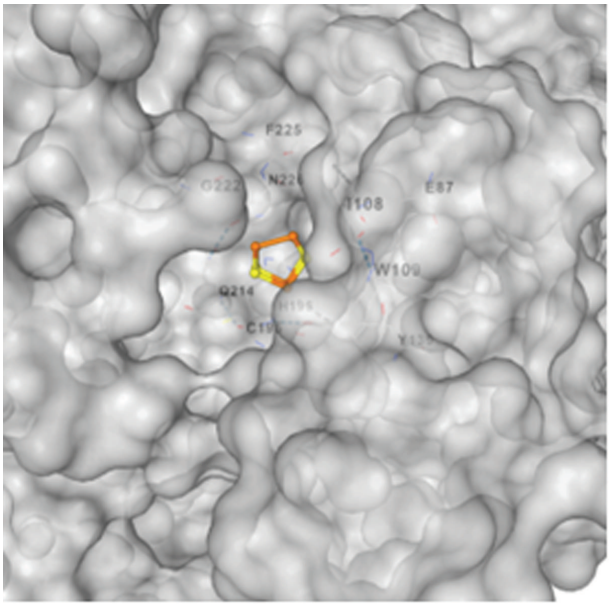



**Fig. 10.** The 3D-binding of interaction of $Co_{0.77}Fe_{0.23}Fe_2O_4/Fe_2O_3$ with 6RKS.

## 4. Conclusion

In conclusion, this study offers a comprehensive exploration into the synthesis, structural elucidation, and functional attributes of $Co_xFe_{1-x}Fe_2O_4/Fe_2O_3$ nanoparticles, where $x$ was precisely controlled to 0.30 and 0.77. The adopted co-precipitation methodology proved efficient for producing these nanocomposites, whose crystallographic, morphological, and magnetic characteristics were rigorously assessed. The key findings include the successful tuning of direct and indirect band gap energies and the observation of near-spherical nanoparticles within a well-defined size range (20.7 nm–23.7 nm), critical parameters for optimizing biomedical applications. Detailed surface characterization, including Hirshfeld analysis, provided further insights into their molecular topology, which, alongside their magnetic responsivity, positions them as versatile candidates for applications ranging from advanced data storage to sophisticated drug delivery platforms. Crucially, the molecular docking studies presented herein offer compelling evidence of interactions between these nanoparticles and DNA gyrase, suggesting a promising trajectory for their exploitation as antimicrobial agents against increasingly prevalent antibiotic-resistant pathogens. This work, therefore, significantly advances the understanding of these tailored nanomaterials, aligning with contemporary efforts to develop innovative solutions for pressing biomedical and environmental concerns.

## References

[1] Tamboli O Y, Patange S M, MohantaY K, Sharma R and Zakde K R 2023 *J. Nanomater.* **2023** 770212
[2] Morais D O, Pancotti A, Souza G S, Saivish M V, Braoios A, Moreli M L, Souza M V B, Costa V G and Wang 2010 *J. Mater. Sci. Mater. Med.* **32** 101
[3] Ashour A H, El-Batal A I, Abdel Maksoud M I A, El-Sayyad G S, Labib Sh, Abdeltwab E and El-Okr M M 2018 *Partic* **40** 141
[4] Harzali H and Azizi M 2024 *J. Environ. Chem. Eng.* **12** 113413
[5] Alcaá O, Bricño S, Brämer-Escamilla W, Silva and Toroidal P 2017 *Mater. Chem. Phys.* **192** 17
[6] Deraz, N and Abd-Elkader O H 2014 *J. Anal. Appl. Pyrol.* **106** 21
[7] El Ghandoor H, Zidan H M, Khalil M MM H and Ismail M I M 2012 *Phys. Scr.* **86** 01540
[8] Wu F, Tian F, Li M, Geng S, Qiu L, He L, Li L, Chen Z, Yu Y, Yang W and Hou Y 2025 *Angew. Chem. Int. Edn.* **64** e202413250
[9] Li L, Tian F, Wu F, Qiu L, Geng S, Li M, Chen Z, Yang W, Liu Y and Yu Y 2025 *Appl. Catal. B Environ.* **361** 124660
[10] Cui S, Wang F and Yang W 2025 *Sens. Actuators B. Chem.* **425** 136996
[11] Tatarchuk T, Bououdina M, Paliychuk N, Yaremiy I and Moklyak V 2017 *J. Alloys Compd.* **694** 77
[12] Kombaiah K, Vijaya J J, Kennedy L J, Bououdina M, Ramalingam R J and Al-Lohedan H A 2018 *Mater. Chem. Phys.* **204** 410
[13] Hammiche-Bellal Y, Djadoun A, Meddour-Boukhobza L, Benadda A, Auroux A, Berger MH and Mernache F 2016 *Mater. Chem. Phys.* **177** 384
[14] Dabagh S, Haris S A and Ertas Y N 2023 *J. Clust. Sci.* **34** 2067
[15] Gheidari D, Mehrdad M, Maleki S and Hosseini S 2020 *Heliyon* **6** e05058
[16] El Ghandoor H, Zidan H M, Khalil M M H and Ismail M I M 2012 *Int. J. Electrochem. Sci.* **7** 5734
[17] Gutierrez F V, Lima I S, De Falco A, Ereias B M, Baffa O, Diego de Abreu Lima C, Morais Sinimbu L I, De la Presa P, Luz-Lima C and Araujo D F J F 2024 *Heliyon* **10** e25781
[18] Moumen N and Pileni M P 1996 *Chem. Mater.* **8** 51128
[19] Li X, Chen G, Po-Lock Y and Kutal C 2002 *J. Mater. Sci. Lett.* **21** 1881
[20] Lacava Z, Azevedo R, Martins E, Lacava L, Freitas M, Garcia V, Rébula C, Lemos A, Sousa M, Tourinho F, Da Silva M and Morais P 1999 *J. Magn. Magn. Mater.* **201** 431
[21] Pinheiro W O, Fascineli M L, Farias G R, Horst F H, Corêa L H, Magalães K G, Sousa M H, Azevedo R B and Lacava M Z G M 1999 *Int. J. Nanomed.* **14** 3375
[22] Schrödinger Maestro Schrödinger. Schrödinger Release 2018-1 2018
[23] Ha N, Van Dat D T and Nguyet T T 2019 *J. Sci. Nat. Sci. Technol.* **35** 55
[24] Cui S Wang F and Yang W 2025 *Sens. Actuators B Chem.* **425** 136996

[25] Gong H, Bao C, Guo X, Tian F, Qiu L and Yang W 2024 *Microchem. J.* **204** 110987

[26] Amel Z, Abdelhafid S, Diana D, Riviere E, Salim O, Jacqueline B and Mehran M 2023 *New J. Chem.* **47** 2626

[27] Schutz D and McCarthy G 1987 *Powder diffraction data* (North Dakota State University) ICDD Grant-in-Aid

[28] Li L, Tian F, Wu F, Qiu L, Geng S, Li M, Chen Z, Yang W, Liu Y and Yu Y 2025 *Appl. Catal. B Environ.* **361** 124660

[29] De Gonález A B and Darby S 2004 *Lancet* **363** 345

[30] Cullity B D and Stock S R 2014 *Elements of X-Ray Diffraction*, 3rd Edn. (New Jersey: Pearson Education) p. 103

[31] Kabbur S M, Waghmare S D, Ghodake U R and Suryavanshi S S 2018 *AIP Conf. Proc.* **1942** 130002

[32] William D, Callister J R and Rethwisch D G 2018 *Materials Science and Engineering: an Introduction*, 10th edn. (New Jersey: John Wiley & Sons, Inc.) p. 409

[33] Rao B P, Caltun O, Cho W S, Kim C O and Kim C G 2007 *J. Magn. Magn. Mater.* **310** e812

[34] Ismail M I M 2018 *Mater. Res. Express* **5** 095004

[35] Arai K I and Ishiyama K 1999 *J. Magn. Magn. Mater.* **133** 1

[36] Davis E A and Mott N F 1970 *Phi. Mag.* **179** 0903

[37] Ismail M I M and Faramawy A M 2024 *Phys. Scr.* **99** 055961

[38] El-Diasty F, El-Sayed H M, El-Hosiny F I and Ismail M I M 2009 *Curr. Opin. Solid State Mater. Sci.* **13** 28

[39] Hassan M A and Hogarth C A 1988 *J. Mater. Sci.* **23** 2500

[40] Spackman P R, Turner M J, McKinnon J J, Wolff S K, Grimwood D J, Jayatilaka D and Spackman M A 2021 *J. Appl. Crystal.* **54** 3

[41] Chavez-Urias I F, López-González L E. Plascencia-Martínez D F, García J J, Flores-Alamo M, Sugich-Miranda R, Medrano F, Picos-Corrales L A, López-Gastélum K-A, Velázquez-Contreras E F and Rocha-Alonzo F 2023 *ACS Omega* **8** 24601

[42] Al-Sulami A I, Alsuwat M H, AlSulami F M H, Ibrahim A M and Elhenawy A A 2024 *Colloid. Surface A* **687** 133408

[43] Shukla R, Mohan T P, Vishalakshic B and Chopra D 2014 *Cryst. Eng. Comm.* **16** 1702

[44] Broeck V A, Lotz C, Ortiz J and Lamour V 2019 *Nat. Commun.* **10** 1